

A STUDY OF EDGE-ON GALAXIES WITH THE HUBBLE SPACE TELESCOPE'S ADVANCED CAMERA FOR SURVEYS. I. INITIAL RESULTS.

ANIL C. SETH
University of Washington

JULIANNE J. DALCANTON*
University of Washington

ROELOF S. DE JONG
Space Telescope Science Institute
Re-Submitted Version, Nov. 8th, 2004

ABSTRACT

We present the initial results of a Hubble Space Telescope/ACS snapshot survey of 16 nearby, edge-on, late-type galaxies covering a range in distance from 2 to 19 Mpc. The images of these galaxies show significant resolved stellar populations. We derive F606W and F814W photometry for >1.2 million stars, and present color-magnitude diagrams which show a mixture of young, intermediate, and old stars in each galaxy. In one of the fields we serendipitously detect stars from the Large Magellanic Cloud. We also identify a candidate young dwarf galaxy lying ~ 2 kpc above the plane of NGC 4631. For the nearest six galaxies, we derive tip of the red giant branch distances and demonstrate that these galaxies fall on the K-band Tully-Fisher relation established in clusters. From the color of the red giant branch, we also find evidence that these galaxies possess a metal-poor thick disk or halo population.

Subject headings: galaxies: distances and redshifts – galaxies: dwarf – galaxies: Magellanic Clouds – galaxies: spiral – galaxies: stellar content – techniques: photometric

1. INTRODUCTION

This paper is the first in a series presenting results from a Hubble Space Telescope (HST) snapshot program of nearby edge-on galaxies. These galaxies are mostly low mass, late-type spirals with circular velocities below 200 km/sec. Although the project was designed to study the dust content of the galaxies, a number of the galaxies were close enough to resolve a significant population of stars and it is the resolved stars that we focus on here. Previous studies of resolved stellar populations with HST have shown that they can be used to answer a variety of questions. The ages and metallicities of the stars can be used to address issues of galaxy formation (e.g. Butler et al. 2004; Brown et al. 2003; Dolphin et al. 2003; Sarajedini & Van Duyne 2001) and distances can be found using the tip of the red giant branch (TRGB) method (e.g. Méndez et al. 2002; Karachentsev et al. 2003a). In this paper we present the galaxies' images, stellar photometry, and some initial results, including TRGB distance measurements, the identification of a possible young dwarf galaxy near NGC 4631, and the detection of LMC stars $\sim 9^\circ$ away from the galaxy center. In the second paper (Paper II, Seth et al. 2004) we analyze the variation in the vertical distribution of different stellar populations and present evidence that many of these galaxies host metal-poor thick disks.

First, in §2 we describe our sample, present a detailed description of our image and photometry data reduction

process, and discuss the stellar models and photometric transformations we use to analyze our data. In §3 we present images and color magnitude diagrams of each galaxy and identify the visible stellar populations. We also identify a candidate dwarf galaxy lying just off the plane of NGC 4631, which appears to contain only young stars. Our method and results for TRGB distance determination are discussed in §4 and conclusions follow in §5.

2. SAMPLE DESCRIPTION & DATA REDUCTION

Our sample consists of 16 galaxies observed with the Advanced Camera for Surveys (ACS) as part of an HST Cycle 12 snapshot project (PI: de Jong, PID: 9765). The sample was selected from the Tully & Fisher (1988) and Karachentsev et al. (1993) catalogs to be edge-on and nearby. Of the 40 fields submitted for observation, 18 fields were observed in 16 separate galaxies.

The properties of each galaxy in the sample is given in Table 1. With the exception of NGC 891 & NGC 4565, the galaxies are all later than Sb and have maximum circular velocities below 200 km/sec. Thus, most have a significantly lower mass than the Milky Way. Based on previously published distances ($m-M_{\text{lit}}$ in Table 1), mostly determined using the Tully-Fisher method, the nearest of the galaxies is NGC 55 (1.8 Mpc (Karachentsev et al. 2003a)) and the most distant is NGC 4183 (19 Mpc (Tully & Pierce 2000)). Assuming these distances, the absolute B band magnitudes of the galaxies range from roughly -16 for NGC 4144 & NGC 5023 to roughly -20.5 for IRAS 06070-6147 & NGC 4565. For comparison, the Large Magellanic Cloud has a absolute B magnitude of

Electronic address: seth@astro.washington.edu
*Alfred P. Sloan Research Fellow
Electronic address: jd@astro.washington.edu
Electronic address: dejong@stsci.edu

TABLE 1
GALAXY SAMPLE PROPERTIES

Galaxy	RA(J2000)	Dec(J2000)	Pos. Ang.	b [deg] ^a	Type	B _T	K _{tot} ^b	V _{max}	V _{recess}	m-M _{lit}
IC 2233	08 13 58.8	+45 44 31	-7.6	33.06	SBcd	13.36	10.75	79	558	29.96 ^f
IC 5052	20 52 02.9	-69 11 45	-38.0	-35.80	SBcd	11.67	8.88	79	598	28.80 ^g
IRAS 06070-6147 ^c	06 07 29.9	-61 48 26	42.7	-28.82	Sc	10.72	8.98	133	1227	31.22 ^h
IRAS 07568-4942 ^d	07 58 15.3	-49 51 13	-26.5	-10.58	SBc	12.36	8.04	142	1119	30.06 ^g
IRAS 09312-3248 ^e	09 33 21.2	-33 02 00	89.7	13.64	Sc	12.71	8.88	98	929	30.61 ^h
NGC 55	00 14 54.4	-39 11 59	-70.0	-75.73	SBm	9.58	6.25	67	131	26.28 ⁱ
NGC 891	02 22 33.0	+42 20 53	22.8	-17.41	Sb	10.83	5.94	214	530	29.61 ^j
NGC 3501	11 02 47.3	+17 59 22	28.1	63.37	Sc	13.67	9.41	136	1132	31.04 ^h
NGC 4144	12 09 58.3	+46 27 28	-77.6	69.01	SBc	12.16	9.39	67	267	27.93 ^g
NGC 4183	12 13 16.8	+43 41 53	-14.0	71.73	Sc	12.94	9.85	103	931	31.35 ^k
NGC 4206	12 15 16.8	+13 01 27	1.0	73.55	Sbc	12.83	9.39	124	712	31.29 ^l
NGC 4244	12 17 29.5	+37 48 28	47.2	77.16	Sc	11.12	7.72	93	244	28.26 ^m
NGC 4517	12 32 45.6	+00 06 56	82.6	62.62	Sc	11.12	7.33	137	1126	29.30 ^f
NGC 4565	12 36 20.7	+25 59 15	-44.8	86.44	Sb	10.58	6.06	227	1228	31.05 ^m
NGC 4631	12 42 07.7	+32 32 33	82.6	84.22	SBcd	9.67	6.47	131	599	28.18 ^f
NGC 5023	13 12 11.7	+44 02 17	27.9	72.58	Sc	12.81	8.74	77	406	28.75 ^f

NOTE. — RA, Dec and Position Angle from K band galaxy fits described in Appendix. All other data from HYPERLEDA/LEDA (Paturel et al. 1995, 2003) except where noted. (a) Galactic latitude, (b) Total K-band magnitude from Jarrett et al. (2003), (c) IRAS 06070-6147 also known as ESO 121-G6, (d) IRAS 07568-4942 also known as ESO 209-G9, (e) IRAS 06070-6147 also known as ESO 373-G8 or UGCA 168, (f) Bottinelli et al. (1985), (g) Bottinelli et al. (1988), (h) assuming $H_0=70$ km/sec, (i) Karachentsev et al. (2003a), (j) Tonry et al. (2001), (k) Tully & Pierce (2000), (l) Gavazzi et al. (1999), (m) Karachentsev et al. (2003b), (n) Jensen et al. (2003)

-17.6, using the B_T magnitude from the LEDA database (Paturel et al. 1995) and assuming a distance modulus of 18.50 (Alves 2004). We also performed model fits to 2MASS K band images to obtain a consistent set of structural properties for use in our analysis. These fits are described in detail in the Appendix. In Table 2 we show the resulting scale length (h_R), scale height (z_0), and half-light height $z_{1/2}$. Note that for the model used (Eq. 1 of the Appendix), $z_{1/2}=0.549z_0$.

The HST imaging was obtained using the Wide Field Camera (WFC) camera of ACS. A total of 18 fields in 16 galaxies were observed with the F606W and F814W filters (see Table 3). Each field was observed with one of two observing plans:

- **2×2:** 14 fields have two exposures of 338 seconds in F606W and two exposures of 350 seconds in F814W.
- **1×2:** 4 fields have one 400 second exposure in F606W and two 338 second exposures in F814W.

In all cases where two exposures were taken, they were dithered to fill in the gap between the two ACS/WFC CCDs.

We developed the following data reduction pipeline for these galaxies:

1. Removal of cosmic rays using the Laplacian edge-detection routine of van Dokkum (2001) on the raw FLT images obtained from the HST/MAST archive.
2. Sky subtraction, drizzling and further cosmic ray removal using the PyRAF ‘multidrizzle’ task (code written by Anton Koekemoer).
3. Location and aperture photometry of objects in the image using DAOPHOT II (Stetson 1987).

4. Determination of the point-spread function (PSF) and PSF photometry also using DAOPHOT II.

5. Artificial star tests to obtain the completeness as a function of position in our images.

All 18 fields were reduced using this same pipeline. Noting the lack of detailed descriptions of ACS data reduction and photometry in the literature, we will now describe each of these steps in detail.

2.1. Cosmic Ray Removal & Drizzling

Based on ACS report 99-09 (Mutchler et al.), we expect to find that approximately 1.5% of pixels ($\sim 300,000$ pixels in our final 4350×4350 images) are affected by cosmic rays. Because our data set includes only two images, we hoped to be able to reject cosmic rays in each single image before combination.

Tests of the Laplacian edge detection method on WFPC2 data found that it was an effective method for removing CRs even on undersampled data (van Dokkum 2001). We therefore adopted the same ‘la_cosmic’ IDL code for our data reduction. However, we found two problems when the method was applied to our data. First, while the code appeared to be very effective at removing cosmic rays, there were also a significant number of obvious false detections in high brightness regions. Second, we found that removed cosmic rays still left small halos behind. To address the false detections we set very stringent limits for what was counted as a cosmic ray (sigclip=6, objlim=8). To remove the residual halos, we expanded the cosmic ray removal to the four nearest neighbors of a detected cosmic ray. Although this undoubtedly removed some pixels unaffected by CRs it also eliminated all signs of the halos around removed CRs. In total, the altered ‘la_cosmic’ routine resulted in the removal and interpolation over $\sim 150,000$ pixels per science image in

TABLE 2
K BAND DISK FIT PARAMETERS

Galaxy	Σ_0 [mag/□′′]	h_R [′′]	z_0 [′′]	h_R/z_0	$z_{1/2}$ [′′]	h_R [pc] ^a	z_0 [pc] ^a
IC 2233	18.42	25.97	6.87	3.78	3.77	1236	327
IC 5052	18.02	53.87	13.35	4.04	7.33	1574	390
IRAS 06070-6147	15.92	16.36	4.07	4.02	2.23	1391	346
IRAS 07568-4942	16.05	27.80	6.87	4.05	3.77	1386	342
IRAS 09312-3248	17.52	38.24	10.33	3.70	5.67	2455	663
NGC 55	17.38	93.30	42.52	2.19	23.34	958	437
NGC 891	15.59	90.75	11.86	7.65	6.51	3676	481
NGC 3501	16.20	19.96	4.15	4.81	2.28	1562	325
NGC 4144	18.01	30.56	12.68	2.41	6.96	1103	458
NGC 4183	17.47	19.66	7.21	2.73	3.96	1775	651
NGC 4206	17.24	24.44	7.45	3.28	4.09	2146	654
NGC 4244	17.91	84.27	22.14	3.81	12.15	1783	469
NGC 4517	17.02	79.13	14.64	5.41	8.04	2779	514
NGC 4565	16.02	87.86	13.67	6.43	7.50	6908	1075
NGC 4631	15.62	35.49	13.74	2.58	7.54	1323	512
NGC 5023	18.16	39.81	9.29	4.29	5.10	1275	298

NOTE. — (a) Derived using distances from Table 1 or when available, Table 5

TABLE 3
OBSERVED HST FIELDS

Field	Obs. Plan ^a	# Stars
IC 2233	2×2	15697
IC 5052	2×2	68636
IRAS 06070-6147	1×2	15271
IRAS 07568-4942	1×2	23582
IRAS 09312-3248	2×2	21667
NGC 55	1×2	281536
NGC 55-DISK	2×2	253108
NGC 891	2×2	33508
NGC 3501	2×2	4887
NGC 4144	2×2	60552
NGC 4183	2×2	13103
NGC 4206	2×2	8733
NGC 4244	2×2	121238
NGC 4517	2×2	49201
NGC 4565	2×2	20192
NGC 4631	2×2	104940
NGC 4631-DISK	2×2	97656
NGC 5023	1×2	42293

NOTE. — (a) **2×2**: denotes fields with two 338 second exposures in F606W and two 350 second exposures in F814W. **1×2**: denotes fields with one 400 second exposure in F606W and two 338 second exposures in F814W.

the FLT files. However it also left behind some obvious cosmic ray features. We note that when we had only one exposure in a filter, we used less stringent parameters for selecting cosmic rays, which may have resulted in the removal of real sources. However, these images were not used for source detections so the only affect of this would be occasionally spurious photometric results.

The remaining cosmic rays were removed in the drizzling process. We ran the PyRAF ‘multidrizzle’ task to create 4350×4350 pixel images. Due to our crowded fields, the default sky subtraction produced obvious mismatches in sky brightness between chip quadrants, requiring us to use skytype=‘single’, which applies a single

sky value to each CCD image. We also found determining the sky value using the mode (skystat=‘mode’) rather than using the median (which is the default), gave better matched sky values. Despite these measures, some of our most crowded fields (e.g. NGC 4631) show a slight mismatch in sky brightness between the two CCDs. This should not affect the identification or photometry of stars in these images because both use locally determined sky values. Comparing the ‘median’, ‘rreject’ and ‘minmed’ modes of image combination, we found the default ‘median’ mode surprisingly yielded the best results for cosmic ray removal. The ‘lanczos3’ kernel was used for creating the final images with a pixel scale of 0.05 arcseconds. We found that the ‘lanczos3’ kernel gave a sharper image than the default ‘square’ kernel. Specifically, within a two pixel aperture, stars in an image made with the ‘lanczos3’ kernel had ~5% more flux than in an image made with a ‘square’ kernel. For apertures larger than four pixels, fluxes in the two images were the same. All further analysis is done with the final, drizzled images.

2.2. Object Identification & Aperture Photometry

All of the galaxies in the sample show a resolved stellar component. Individual stars were detected using the FIND routine in DAOPHOT II (Stetson 1987) with a threshold of 5σ over the local background. The routine initially returned anywhere from 15,000 sources in IRAS 06070-6147 to 400,000 sources in NGC 55. The final number of sources, shown in Table 3, count only sources detected in both filters. For the 1×2 fields, we detected objects only in the F814W filter and then used that source list for both filters.

We performed aperture photometry using the PHOT routine with an aperture of 4 pixels and a sky annulus between 11 and 14 pixels. We then compiled the photometry in both filters and required objects be detected independently in both filters for the 2×2 fields. This reduced the number of objects by 40-75% from the original source lists. We note that there was a ~0.3 pixel positional offset between the F606W and F814W drizzled

images in all the observations. After correcting for this offset we matched objects within 1 pixel of each other in the two filters. In the very small number of cases where more than one source was found within one pixel, the brighter match was used. As noted above, in the 1×2 fields, sources were found only in the F814W band – the positions from the F814W image were then used for both filters to determine the aperture magnitudes.

We transformed all of our photometric data to the VEGAmag system using provided zeropoints (ACS ISR 2004-8, De Marchi et al.) and aperture corrections (M. Sirianni, private communication). The zeropoints provided are for an infinite aperture and the aperture corrections give the aperture correction from a 10 pixel to infinite aperture. We derived a correction from a 4 to 10 pixel aperture using isolated bright stars from the 2×2 fields. The resulting corrections showed very little (<0.01 mag.) scatter and are shown in Table 4 along with the zeropoints and $10-\infty$ aperture corrections.

2.3. PSF photometry

All of the galaxy images are very crowded, greatly reducing the accuracy of aperture photometry. To improve the photometry, we modeled the PSF in our drizzled fields. An adequate model for the ACS/WFC PSF must allow for spatial variations of the PSF over the wide field of view. Fortunately, DAOPHOT II has the capability to model the PSF as a combination of an analytical function and empirical sub-pixel corrections that depend quadratically on the position in the field.

Initially we attempted to model the PSF in each field independently, but found that the derived PSFs were greatly limited by the small numbers of bright, isolated stars (typically 50) available in the large 4350×4350 pixel frames. Instead we assumed that the PSF was roughly constant over the course of our observations and constructed a patchwork image in each filter using bright, isolated stars from the 2×2 fields. The resulting images contained ~ 700 stars and enabled more accurate determination of the spatial variation of the PSF. Out of the options given by DAOPHOT II, the best fitting analytical functions in both filters were Moffat functions, $f(x) = 1/(1 + (r/\alpha^2))^\beta$. In the F606W filter, $\alpha = 0.76$ and $\beta = 2.5$, while in F814W $\alpha = 0.63$ and $\beta = 1.5$. The FWHM of these analytical functions is 0.86 pixels (0.043 arcsec) in F606W and 0.97 pixels (0.049 arcsec) in F814W. Based on a comparison between a variable and constant PSF, the spatial corrections in our PSF affect the photometry by at most 0.03 magnitudes. The correction of PSF magnitudes to 10 pixel aperture photometry is given in Table 4. The accuracy of these corrections is ~ 0.03 magnitudes. We treat this as a systematic error, and do not include it in individual errors of the stars. The computed PSF has a radius of 7 pixels (0.35 arcsec).

Figure 1a shows the resulting PSF magnitude color-magnitude diagram (CMD) for the NGC 55-DISK field. The NGC 55-DISK field CMD is the cleanest of our CMDs due to the galaxy’s proximity and the field’s relative lack of dust. The clear features seen in this CMD, which will be discussed in §3, demonstrate the quality of our photometry.

2.4. Artificial Star Tests

To assess the completeness limit as a function of position, magnitude, and color, we inserted large numbers of artificial stars in our images and then attempted to recover them with our data reduction pipeline. These stars were input in grids separated by 20 pixels with an overall random position offset. In this way, $\sim 38,000$ stars were added to a field, each with a random F606W VEGAmag between 18 and 29 and a F606W-F814W color between -1.0 and 3.0. We then ran the stars through a pipeline identical to the one outlined above for finding stars and determining their photometry. This was done with different random position offsets to generate as many as four million artificial stars distributed throughout each field. The large computing time required to run these tests was enabled through use of the distributed computing system, Condor¹.

Figure 2 shows the completeness as a function of scale height in NGC 4244 for stars at a variety of magnitudes. Away from the plane of the galaxy, in a non-crowded area, the 50% completeness level of our data is ~ 27 mag in F606W and ~ 26 mag in F814W. However, the crowding in the midplane of the galaxy drastically reduces the completeness, by as much as 35% at moderate magnitudes. Note that Figure 2 contains the results from artificial stars of all colors, but for a specific range in color the completeness can be higher or lower. For instance, the F814W 50% completeness in non-crowded areas at F606W-F814W between -1 and 1 is ~ 26.5 , but rises steeply at redder colors. Figure 3 shows a typical 20% completeness line as a function of color in each of the color-magnitude diagrams. The scatter from galaxy to galaxy in the completeness values is a few tenths of a magnitude.

2.5. Stellar Models & Photometric Transformations

Critical to the interpretation of our data is the ability to connect the ACS VEGA magnitude system for the F606W and F814W filters with existing stellar models and previous data. We rely on two sources for performing this photometric transformation. First, we used a set of the Padova isochrones and single stellar population models transformed into the ACS VEGAmag system using synthetic spectra and ACS/WFC instrument response (L. Girardi, private communication). These models are the standard Girardi et al. (2000) isochrones with tracks at $Z=0.0001, 0.0004, 0.001, 0.004, 0.008, \& 0.019$ ($[\text{Fe}/\text{H}]=-2.3, -1.7, -1.3, -0.7, -0.4, 0.0$) with ages between 4 Myr and 18 Gyr.

Second, in very limited cases, we used transformations from the ACS VEGAmag system to Johnson V & I provided by M. Sirianni (private communication). However, these transformations are potentially inaccurate as they attempt to infer the spectrum of a star from limited color information and are valid only for $-0.5 < V-I < 2.3$.

The VEGAmag F606W-F814W color is similar to Johnson V-I, but has a somewhat smaller wavelength span, meaning that the differences in color are somewhat more moderate. For instance, Red Giant Branch stars are ~ 0.3 magnitudes bluer in F606W-F814W [VEGA-

¹ The Condor Software Program (Condor) was developed by the Condor Team at the Computer Sciences Department of the University of Wisconsin-Madison. All rights, title, and interest in Condor are owned by the Condor Team.

TABLE 4
PHOTOMETRIC CONSTANTS

Filter	Zeropoint [mag]	10-∞ Ap. Cor. [mag]	4-10 Ap. Cor. [mag]	PSF-10 Cor. [mag]
F606W	26.398	0.091±0.001	0.079±0.006	0.017±0.027
F814W	25.501	0.090±0.001	0.095±0.009	0.019±0.025

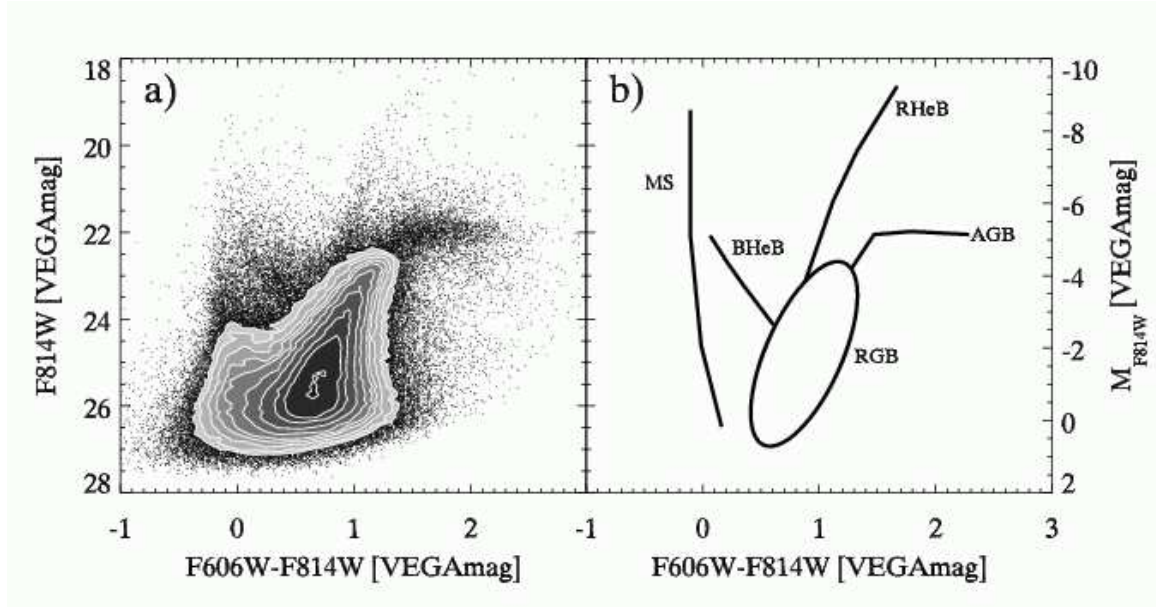


FIG. 1.— (a) Color-Magnitude Diagram (CMD) of the 253,108 stars in the NGC 55-DISK field. Contours are used where the density of points becomes high. The contours are drawn at densities of 75, 100, 150, 200, 250, 350, 500, 750, 1000, and 1500 stars per 0.1 magnitude and color bin. (b) Cartoon CMD showing the location of Main Sequence (MS), Red Giant Branch (RGB), Asymptotic Giant Branch (AGB), Red Helium Burning Sequence (RHeB), and Blue Helium Burning Sequence (BHeB) each of which is described in §3.

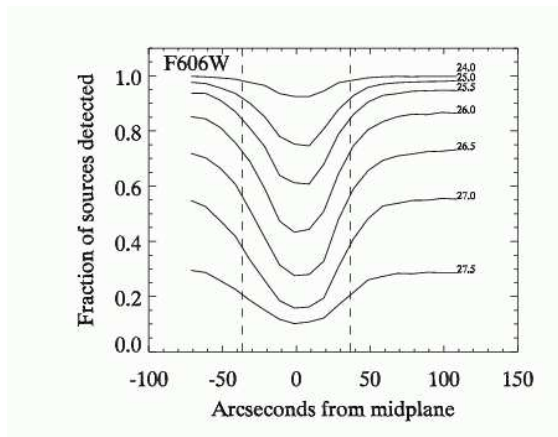


FIG. 2.— The fraction of artificial stars detected as a function height above the midplane of the galaxy in NGC 4244. The lines give the completeness in 0.5 mag wide bins around a magnitude shown on the right-hand side. Dashed lines show $\pm 3z_{1/2}$, the minimum height used for the TRGB determination in §4.

mag] than in V-I. Unless explicitly stated otherwise, all magnitudes in the paper are in the VEGAmag system.

3. COLOR-MAGNITUDE DIAGRAMS

In the sample as a whole we have determined photometry for over 1.2 million objects (see Table 3), a vast majority of which are stars in the sample galaxies.

Figure 3 shows images and color-magnitude diagrams (CMDs) of each of the galaxies. The CMDs show all the stars detected in each field. Of all the CMDs in our sample, the NGC 55-DISK CMD reaches the faintest absolute magnitudes. In Figure 1b we illustrate the distinct features visible in its CMD. Many of the other CMDs in Figure 3 share these features at fainter apparent magnitudes. These visible features are due to the following stellar populations:

- Main Sequence (MS) - At the bright absolute magnitudes at which we are observing ($M_{F814} < 0$), MS stars are younger than a few 100 Myr. At the bright end, the MS and Blue Helium Burning sequence overlap.
- Red and Blue Helium Burning Sequences (RHeB and BHeB) - These sequences contain young massive stars undergoing core helium burning. Along both these sequences, the ages and masses of the stars are proportional to the luminosity, with younger, more massive stars populating the bright end. The faintest stars along the RHeB have an age of ~ 200 Myr, while the BHeB branch extends down to ~ 600 Myr (Dohm-Palmer et al.

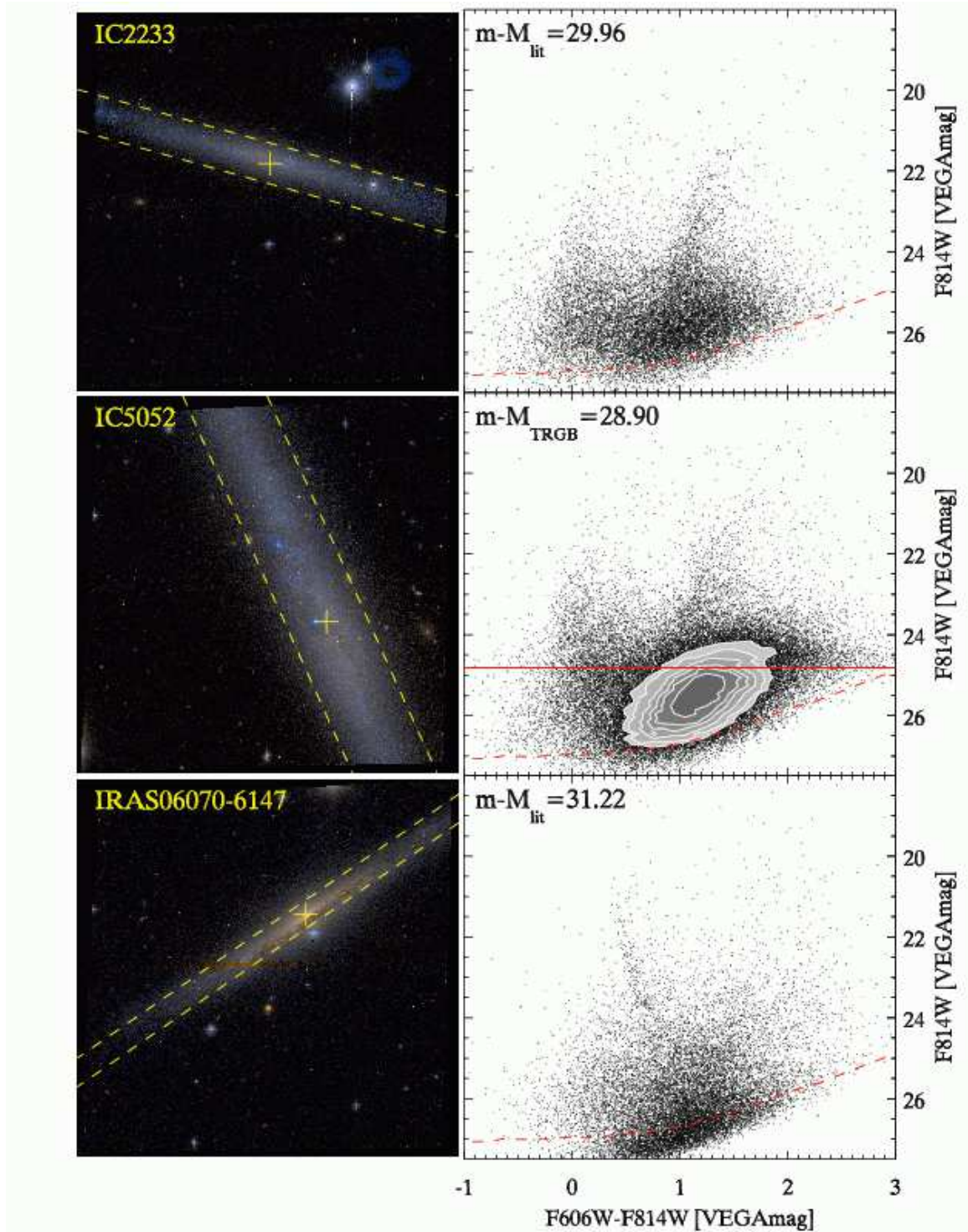
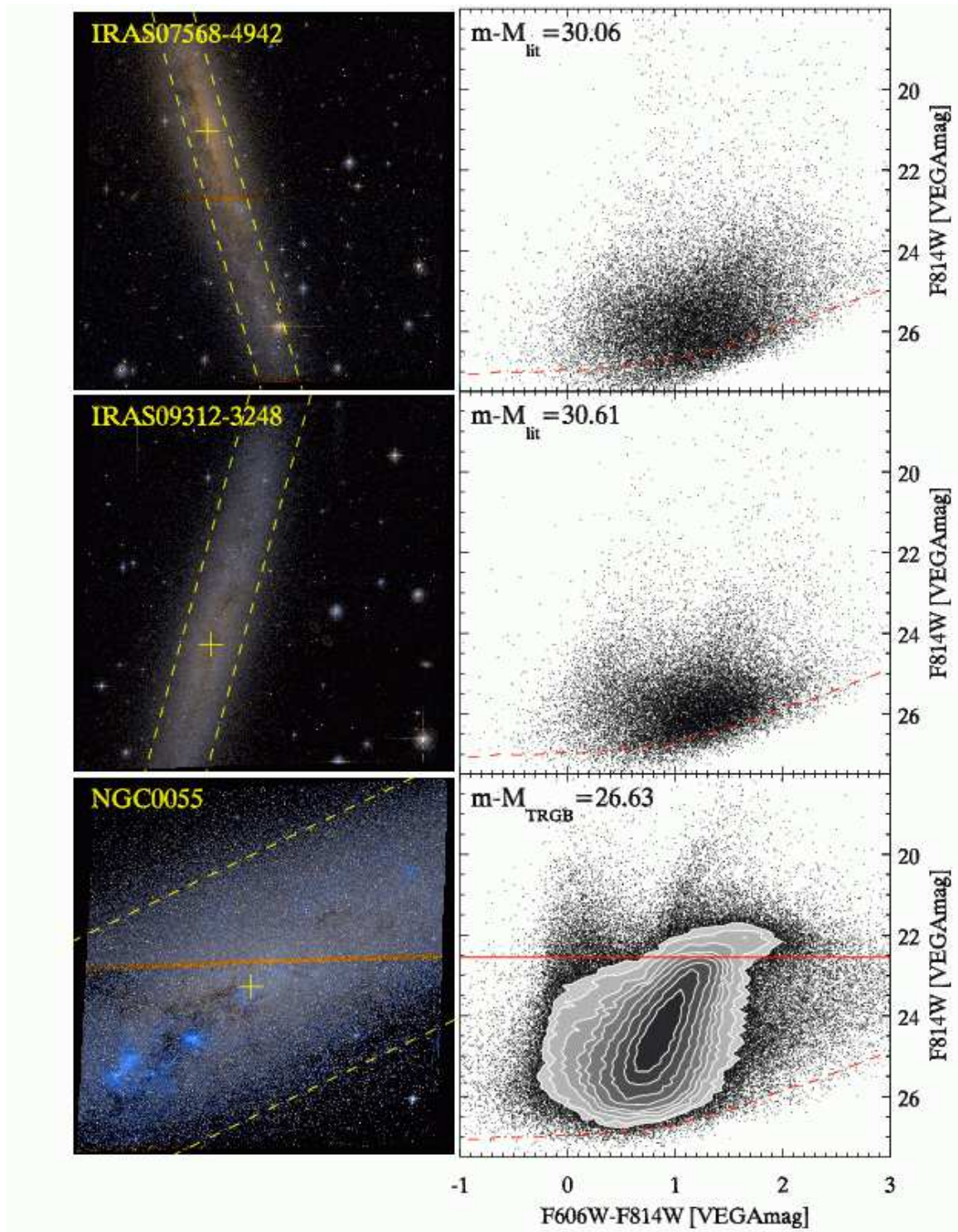
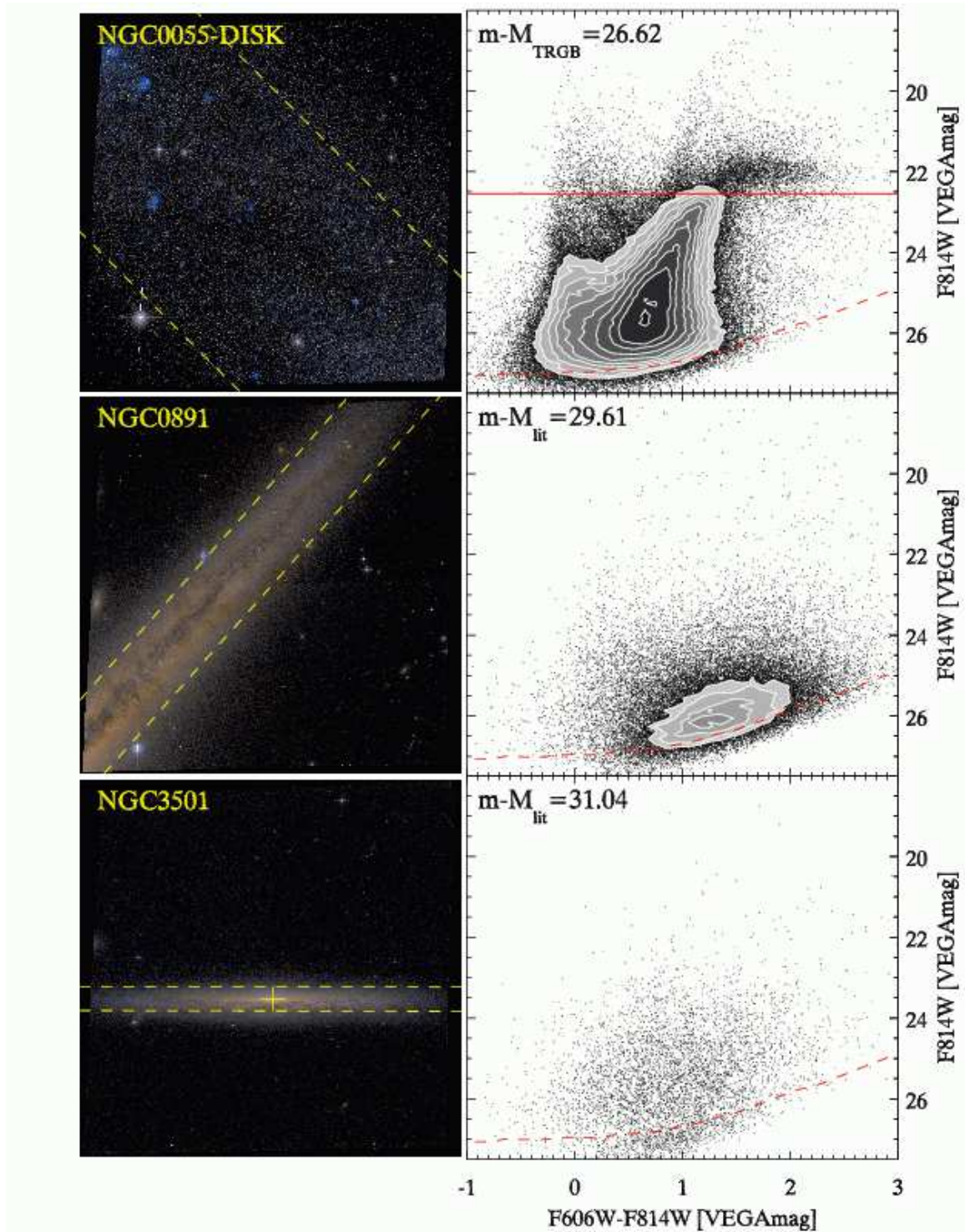


FIG. 3.— (*left*) – Combined F606W and F814W images of each field. Dashed lines indicate $3z_{1/2}$ and cross indicates galaxy center as determined from fits to K band 2MASS data (see Appendix). The images are $218'' \times 218''$. The box shown in the NGC 4631-DISK field gives the location of image shown in Fig. 4. Note that color images of these pictures are presented in the electronic version. (*right*) – Color magnitude diagrams of all the objects in each field. Contours are shown where densities exceed 75 stars per 0.1 magnitude and color bin. Contours have the same levels as those shown in Fig. 1. The dashed line indicates the typical 20% completeness limit. The solid horizontal line (when present) indicates the TRGB. The nearly vertical feature at $F606W-F814W \sim 0.4$ in IRAS 06070-6147 is due to LMC field stars. Distance moduli $m-M_{\text{lit}}$ or $m-M_{\text{TRGB}}$ come from Tables 1 and 5.

FIG. 3.— *continued*

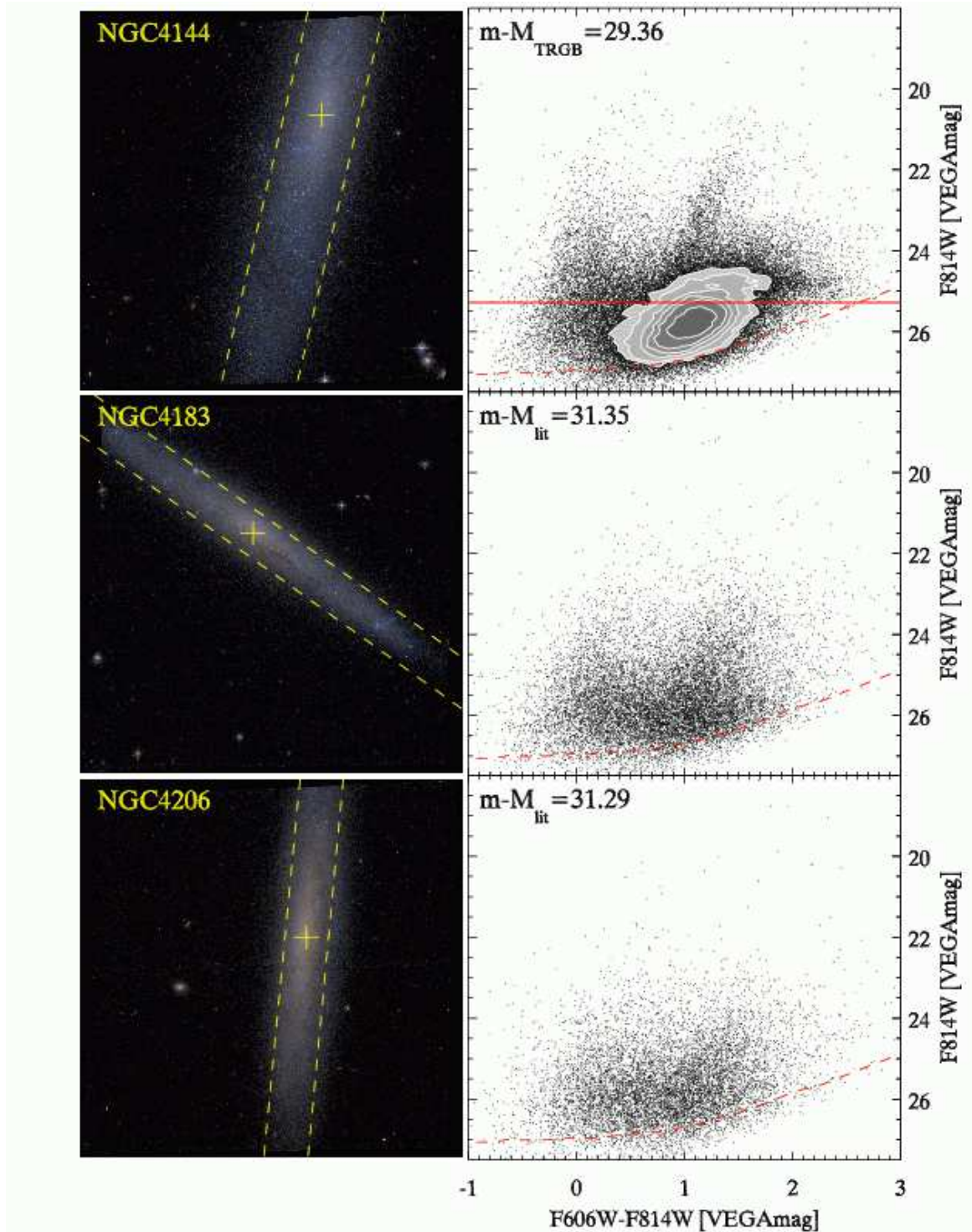
FIG. 3.— *continued*

2002; Dohm-Palmer & Skillman 2002).

- Asymptotic Giant Branch (AGB) - The AGB contains stars of intermediate age, after completion of their core-helium burning stage. The observed portion of the AGB is brighter and redder than the RGB. Based on the Girardi isochrones, the AGB stars observed here mostly have metallicities be-

tween $[\text{Fe}/\text{H}] = -0.7$ and 0.0 and ages between 100 Myr and a few Gyr. At absolute magnitudes fainter than the red giant branch tip $M_{\text{F814W}} \sim -4$ the AGB stars cannot be distinguished from the RGB stars

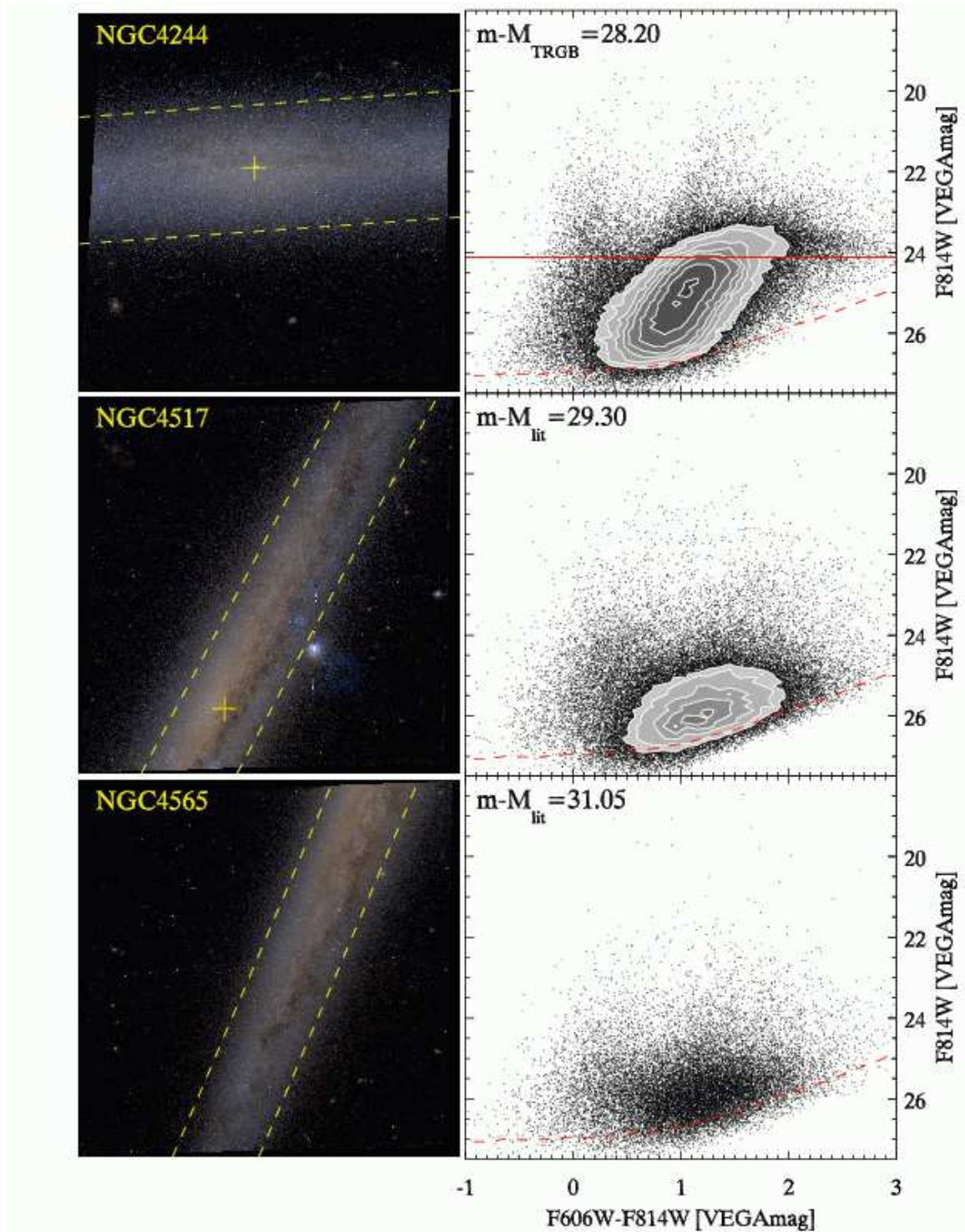
- Red Giant Branch (RGB) - The RGB is dominated by old stars undergoing shell-hydrogen burn-

FIG. 3.— *continued*

ing. These stars have ages > 1 Gyr and represent the oldest of the components visible in our CMDs. The exact position of the RGB depends primarily on metallicity, with more metal-rich stars being redder and fainter in our CMDs.

Inspection of Figure 3 shows that most of these components are clearly visible in IC 2233, IC 5052, NGC 55 (both fields), NGC 4144, NGC 4244, NGC 4631-DISK,

and NGC 5023. These CMDs clearly show evidence for both young and old stellar populations. The effects of dust are also obvious when comparing the color magnitude diagrams of the central NGC 55 and NGC 4631 fields with those taken further out in the disk (NGC 55-DISK and NGC 4631-DISK). In both cases the central CMDs show significant redward blurring of the MS and RHeB, both of which are more clearly detected in the

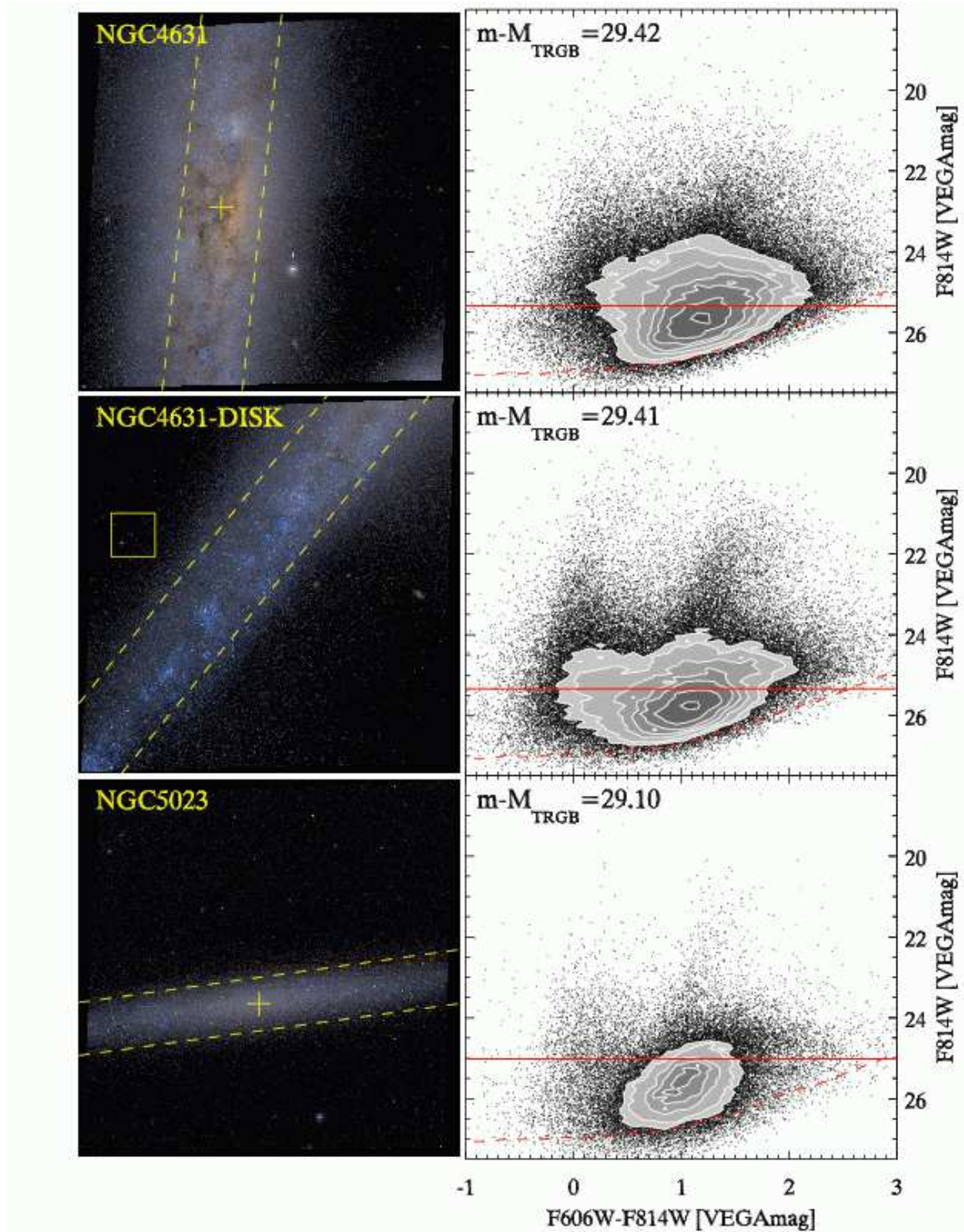
FIG. 3.— *continued*

less obscured ‘-DISK’ fields.

We note that a vast majority of stars detected in each field appear to be in the target galaxies. This can be seen in the clarity of their CMDs and from the spatial distribution of the stars (see Paper II). A significant population of Galactic foreground stars are visible in the CMDs of the three galaxies with the lowest galactic latitudes (see Table 1), IRAS 07568-4942, IRAS 09312-3248 and

NGC 891. They are seen most prominently at $F606W-F814W > 0.5$ and $F814W < 23$.

Before discussing distance measurements using the RGB tip in §4, we briefly discuss two unusual features seen in the CMDs of IRAS 06070-6147 and NGC 4631-DISK. All further interpretation of the CMDs will be presented in Paper II, in which we examine the vertical distribution of the different stellar populations and

FIG. 3.— *continued*

find evidence for old and metal poor thick-disks in these galaxies.

3.1. A Detection of the Large Magellanic Cloud (LMC)

One unusual feature is found in the CMD of IRAS 06070-6147. In the CMD, a clear locus of points can be seen extending between 20th and 24th magnitude and at a color of ~ 0.5 . These are field LMC stars found ~ 9

degrees (8 kpc) from the LMC center, near the outermost clusters associated with the LMC (Irwin 1991).

These stars fit well to isochrones with a distance modulus of 18.5 (Alves 2004), an age of a few Gyr, and metallicities of $[\text{Fe}/\text{H}] = -0.4$ to 0.0. This provides a serendipitous confirmation of the accuracy of our photometric calibration and isochrone bandpass transformation. It also agrees with recent work by Gallart et al. (2004) which

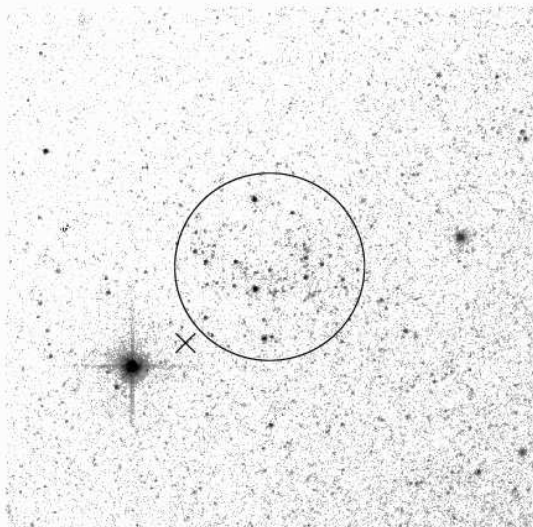


FIG. 4.— An F606W image showing a close-up of the section of NGC 4631-DISK shown as a box in Figure 3. The circle has a radius of $4.5''$ and is centered at $\alpha = 12\text{h}41\text{m}50.30\text{s}$ and $\delta = 32^\circ 31' 1.9''$. The X marks the location of previously identified galaxy NGP9 F268-1993301 (Odewahn & Aldering 1995). A clear overdensity of stars is seen inside the circle.

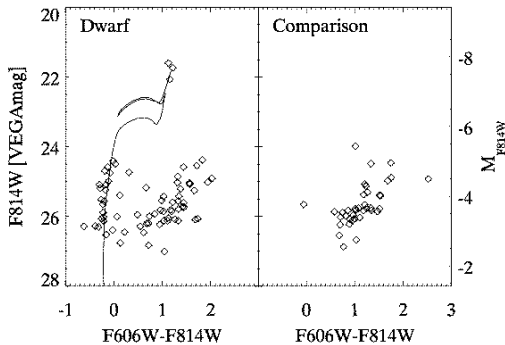


FIG. 5.— (left) — A CMD of the stars inside the circle shown in Figure 4. Overplotted is an isochrone with an age of 30 Myr and $[\text{Fe}/\text{H}] = -0.7$. (right) — The CMD of a comparison field located at the same galactic latitude as the dwarf, but offset a short distance in the longitudinal direction. An absolute magnitude scale is shown assuming $m-M=29.42$.

suggests that the extended ‘halo’ of the LMC is made up of stars as young as ~ 2.5 Gyr.

3.2. A Young Dwarf Galaxy Candidate in NGC 4631

Inspection of the NGC 4631-DISK field image showed a small object marked by a grouping of blue stars sitting significantly off the plane of the disk. This object is shown in Figure 4 and is centered at $\alpha = 12\text{h}41\text{m}50.30\text{s}$ and $\delta = 32^\circ 31' 1.9''$. The object seems to be contained within a radius of $4.5''$ as shown in Fig. 4. Assuming a distance modulus of 29.42 to the object, this gives a radius of ~ 170 pc. The object is located ~ 2 kpc above the plane of NGC 4631. Based on its size, which is too large to be a star cluster, we identify this object as a dwarf galaxy candidate, NGC 4631 DwA (dwarf A).

This dwarf may have been previously discovered by Odewahn & Aldering (1995) with the name NGP9 F268-

1993301 using POSS-I plates. However, their position ($\alpha = 12\text{h}41\text{m}49.89\text{s}$ $\delta = +32^\circ 31' 00.5''$, shown with an X in Fig. 4) and red color (O-E ~ 2) suggests that they suffered from confusion with the bright red star (most likely a foreground object) seen to the lower left of the circle in Figure 4.

The left panel of Figure 5 shows the color-magnitude diagram of the stars in the circle shown in Figure 4. For comparison, we show a field CMD at the same height above the plane of NGC 4631 but offset in the longitudinal direction. NGC 4631 DwA shows a clear overdensity of blue stars. To show this quantitatively, we compare the stars in the dwarf to those within the same range of height above the plane, but lying outside the dwarf, yielding an area ~ 18 times the area of the dwarf. We find 26 stars bluer than $F606\text{W}-F814\text{W}=0.3$ associated with the dwarf, but only 15 in the entire area outside the dwarf. This gives an expected rate ~ 0.8 stars bluer than $F606\text{W}-F814\text{W}=0.3$ in the field of the dwarf, implying that the dwarf has a >30 times overdensity of blue stars. By contrast, the expected rate for stars redder than $F606\text{W}-F814\text{W}$ of 0.3 in the field of the dwarf is ~ 50 stars, while the dwarf contains only 47. This suggests that if any old population exists, it is small enough to contain few stars near the tip of the RGB. The good fit of the isochrone shown in Figure 5 to the blue stars and the bright red stars (probably RHeB stars) in the dwarf suggests an age of ~ 30 Myr. We found that isochrones with a wide range of metallicities and ages between 10-50 Myr can also fit the data quite well. These tests also suggest that the dwarf is located at the same distance modulus (assumed to be 29.42) as NGC 4631.

We can also calculate the integrated magnitudes of NGC 4631 DwA to compare to single stellar population models. The total flux from the dwarf is measured by aperture photometry using an aperture of $4.5''$ and a sky annulus between $5''$ and $6''$. The contribution from NGC 4631’s field stars is then determined by finding the flux using the same aperture and sky annulus at 100 random positions with the same height above the plane, but avoiding NGC 4631 DwA and the bright star visible just to its lower left in Figure 4. The mean of these we use as a background and the standard deviation is the error in this background. The final flux for the dwarf is determined by subtracting off the background and the final error combines the dwarf’s error in the flux with the error in the background. Using this error and the background subtracted flux we find that the F606W magnitude is 20.7 ± 0.2 (a 5σ detection) while the F814W magnitude is 20.3 ± 0.4 (a 3σ detection). These magnitudes correspond to surface brightnesses of 25.2 mag arcsec $^{-2}$ in F606W and 24.8 mag arcsec $^{-2}$ in F814W. Assuming an age of 30 Myr and $[\text{Fe}/\text{H}] = -0.7$, we find a mass of $2.2 \pm 0.4 \times 10^4 M_\odot$ from single the stellar population models (see §2.5). We note that despite being rather uncertain, the F606W-F814W color of 0.4 matches the expected value from this single stellar population, suggesting that any existing older population does not make a significant contribution to the total luminosity of NGC 4631 DwA. The dwarf’s absolute magnitude, $M_{F606\text{W}} = -8.7$ is only slightly brighter than the recently discovered ‘faintest galaxy’ Andromeda IX (Zucker et al. 2004).

The properties of NGC 4631 DwA – a radius of 170

pc, an age of ~ 30 Myr, and a mass of $\sim 2 \times 10^4 M_{\odot}$ are most similar to an OB association. However its location ~ 2 kpc above the disk makes it unusual. If the object is indeed bound it would have a circular velocity of ~ 7 km/sec. However given that the only stars we see are young, it is possible that it is an unbound and gradually dissolving object.

One possible explanation for the creation of this object is that it is caused by a condensation of gas interacting with NGC 4631. Figures 4 and 5 of Rand (1994) show five HI spurs surrounding NGC 4631. Although none of their positions overlap with the position of the dwarf, two spurs meet up with the disk at a position just opposite the dwarf. This explanation for the formation of the object would make it akin to young tidal dwarf galaxies and clusters observed in the tails of interacting galaxies (e.g. Schweizer 1978; Duc & Mirabel 1998; Temporin et al. 2003). Higher resolution HI observations would make it possible to determine if the object is affiliated with a tidal tail.

4. TRGB DISTANCES

The tip of the red giant branch (TRGB) method can be used to determine distances to objects with an old and metal poor ($[\text{Fe}/\text{H}] < -0.7$) resolved stellar population. Of the sample of galaxies presented here, eight fields in six galaxies were close enough to clearly distinguish an RGB tip. To determine the TRGB magnitude we use the discontinuity detection method as presented in Méndez et al. (2002).

4.1. Star selection and method

Before considering the method by which we determine the TRGB, we need to refine the sample of stars. To prevent our result from being affected by *in situ* dust and young stellar populations and to avoid incompleteness (Fig. 2), we consider stars only above $3|z_{1/2}|$. This height is above $>90\%$ of the K band light on the 2MASS images and is above any obvious dust features on our images, except in NGC 4631 which is known to have a large extraplanar dust component (Howk & Savage 1999). The CMDs constructed from these stars show the presence of very few young stars. This can be seen in Figure 6, which shows the CMD of stars above $3|z_{1/2}|$ except in NGC 4631 and NGC 4631-DISK fields where we used a lower limit of $7|z_{1/2}|$ in order to better avoid the dust, crowding and young stellar populations seen at lower scale heights. For the NGC 4631 field, we also used an upper limit of $10|z_{1/2}|$ to avoid stars in the nearby companion, NGC 4627.

Comparison of the CMDs in Fig. 6 to the full field CMD in Figure 3 shows the lack of young RHeB stars and the greater clarity of the RGB due to a lack of crowding. After selecting these stars, we correct their magnitudes for foreground extinction using Schlegel et al. (1998) values for $E(\text{B}-\text{V})$ and assuming $A_{\text{F814W}} = 2.716 \times E(\text{B}-\text{V})$ and $A_{\text{F606W}} = 1.796 \times E(\text{B}-\text{V})$. Finally, we make a color cut ($0.3 < \text{F606W}-\text{F814W} < 1.6$) to eliminate contamination of the upper main sequence and redder AGB stars.

Figure 7 graphically shows the method used to determine TRGB magnitude and error in each field. Using the magnitudes and errors of the selected stars, we construct a Gaussian-smoothed luminosity function, to which each star contributes a unit area Gaussian with

the width determined by the error (see Appendix A of Sakai et al. 1996). This is shown in the top panels of Figure 7. The tip of the red giant branch can be seen as a sudden increase in the luminosity function at a given F814W magnitude. This magnitude can be quantitatively determined using an edge-detection algorithm. We use the logarithmic edge-detection algorithm presented in Méndez et al. (2002). The response of this edge-detection algorithm is shown in the middle panels of Figure 7. Finally, random errors in the TRGB magnitude are determined using a Monte Carlo style simulation where the TRGB magnitude is determined 500 times for stellar magnitudes which have been randomly resampled with replacement. We also include the magnitude errors by adding a Gaussian random error scaled by each stars photometric error. The width of a Gaussian fit to the determined TRGB magnitudes gives us the uncertainty of the derived TRGB value (Méndez et al. 2002). A histogram of these Monte Carlo tests can be seen in the bottom panels of Figure 7.

4.2. TRGB magnitudes

The results of the TRGB determination for the eight fields in which a clear RGB could be distinguished are shown in Table 5 and in the CMDs in Fig. 6. The F814W TRGB magnitudes range from 22.54 for NGC 55 to 25.34 for NGC 4631. The uncertainties are typically ~ 0.03 magnitudes, comparable to the errors found using a similar method in Méndez et al. (2002) and to the systematic errors in our magnitudes (§2.3). In all cases, the value derived for the TRGB fell within one sigma of the Gaussian fitted to the Monte Carlo tests. The second column of Table 5 shows the number of stars used in the TRGB determination of each galaxy.

For each of the galaxies shown in Table 5, a clear TRGB is seen (Fig. 6). For the other galaxies, we are limited in our ability to determine TRGB distances by incompleteness. The F814W 90% completeness level is ~ 25.5 in uncrowded areas at RGB colors and drops off quickly towards fainter magnitudes. The only two other possible detections are NGC 891 and NGC 4517, both of which we measured to have TRGB magnitudes of 25.60. However, examination of the CMDs reveals that it is impossible to exclude the possibility that the stars below that magnitude are AGB or RHeB stars. In addition, the Monte Carlo tests find a wide range of values for the TRGB and their results are not consistent with the a TRGB magnitude of 25.60. We suggest that the derived TRGB magnitude for these galaxies is a lower limit. For the other 8 fields in our sample, there were typically too few stars above $3|z_{1/2}|$ to distinguish any red giant branch.

4.3. Distance Moduli

The I-band absolute magnitude of the TRGB has been found to be at $M_I \sim -4$ via many methods (e.g. Méndez et al. 2002; Lee et al. 1993; Ferrarese et al. 2000). Because the photometric system we use is similar to the Johnson system, we can expect that the TRGB is at a similar F814W absolute magnitude (M_{F814W}). In order to accurately determine the distance, we need to (a) determine the observed TRGB magnitude in the Johnson I system, or (b) determine the exact value M_{F814W} of the TRGB. We take both of these approaches below.

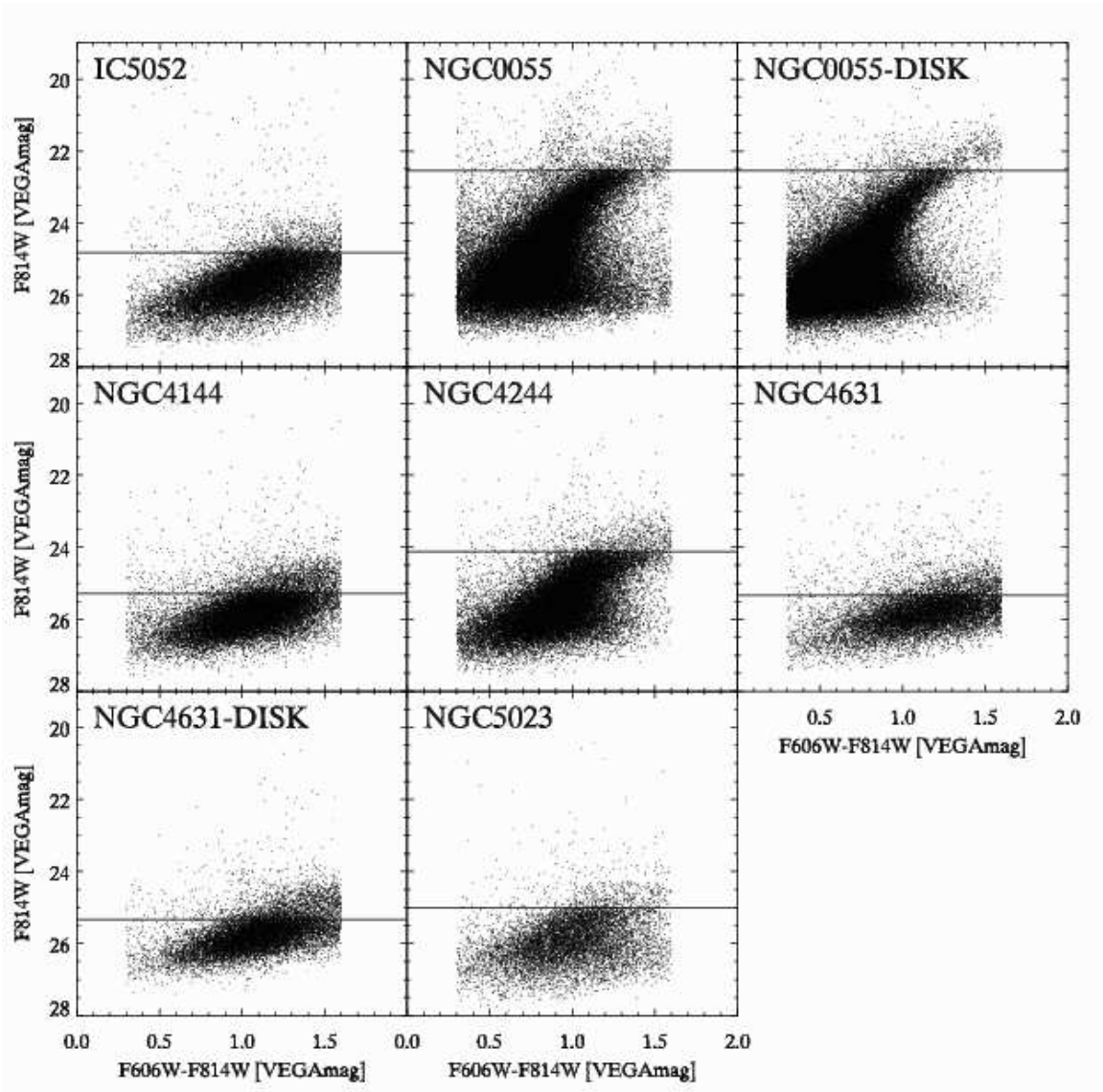


FIG. 6.— The CMDs of stars used in TRGB determination. The line in each pane indicates the magnitude found for the TRGB. Stars were selected to have $0.3 < F606W - F814W < 1.6$, and to be well above the plane of the galaxy ($> 3z_{1/2}$ for all galaxies other than NGC 4631). These CMDs show a much greater clarity than those in Fig. 3 because of the reduced effects of dust and crowding.

TABLE 5
TRGB RESULTS

Field	# of stars used	$F814W_{\text{TRGB}}$ [VEGAmag]	I_{TRGB} [Johnson]	$(F606W - F814W)_{-3.5}$ [VEGAmag]	$(V - I)_{-3.5}$ [Johnson]	[Fe/H]	$m - M_{\text{TRGB}}$
IC 5052	18974	24.82 ± 0.03	24.84 ± 0.04	1.15	1.48	-1.22	28.90
NGC 55	53984	22.55 ± 0.03	22.55 ± 0.03	1.08	1.42	-1.41	26.63
NGC 55-DISK	56651	22.54 ± 0.03	22.55 ± 0.03	1.04	1.36	-1.62	26.62
NGC 4144	19132	25.28 ± 0.02	25.29 ± 0.03	1.06	1.39	-1.50	29.36
NGC 4244	27797	24.12 ± 0.03	24.14 ± 0.03	1.08	1.41	-1.45	28.20
NGC 4631	11204	25.34 ± 0.03	25.37 ± 0.03	1.13	1.47	-1.25	29.42
NGC 4631-DISK	12058	25.33 ± 0.03	25.36 ± 0.04	1.06	1.38	-1.54	29.41
NGC 5023	8376	25.02 ± 0.03	25.04 ± 0.03	1.03	1.33	-1.71	29.10

Using the transformations provided to us by Sirianni, we transformed the stellar data for each galaxy to the V and I filter and redetermined the TRGB exactly the same as above, but using V-I cuts of 0.5 and

1.9. The results are shown in Table 5. By calibrating the TRGB with Cepheid distances, Ferrarese et al. (2000), found the TRGB to be at $M_I = -4.06 \pm 0.07$ (random) ± 0.13 (systematic). The magnitudes of I_{TRGB}

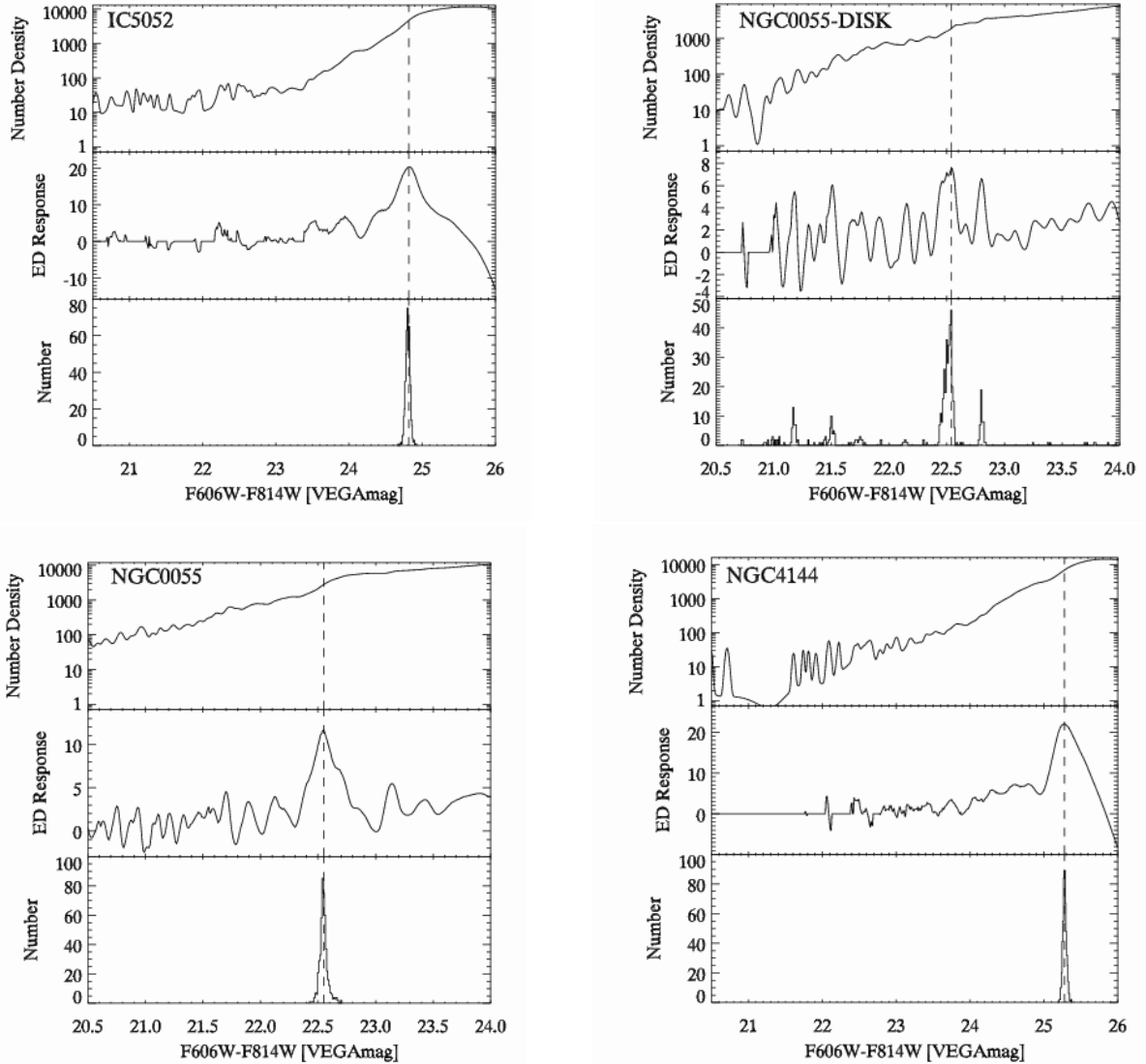


FIG. 7.— TRGB determination for eight fields in six galaxies. In each plot, the top panel shows the Gaussian-smoothed luminosity function as a function of the F814W magnitude, the middle panel shows the edge detection response to the luminosity function and the bottom panel shows a histogram of the edge-detection peak for 500 monte carlo simulations. The dashed line gives the position of the determined TRGB value. For more details see §4.1.

agree with $F814W_{\text{TRGB}}$ to within 0.03 magnitudes for each of the 8 fields, but on average I_{TRGB} is fainter by ~ 0.02 magnitudes. This suggests that the TRGB is at $M_{F814W} \sim -4.08$.

Alternately, we can use the theoretical Padova isochrones (see §2.5), which exist in both filter systems. For both sets of isochrones we take all tracks older than 2 Gyr and with $[\text{Fe}/\text{H}]$ between -2.3 and -0.7. Figure 8 plots the cumulative distribution of the TRGB magnitude in both the F814W VEGAmag system (solid) and in Johnson I (dashed). A great majority of the tracks have TRGB values in both systems between -3.8 and -4.1. The mean, median and brightest values of the absolute magnitude of the TRGB are all ~ 0.03 magnitudes brighter in F814W VEGAmag than in Johnson I, in good agreement with the empirical calibration above. We therefore assume that $M_{F814W} = -4.08$ for determining distances from the observed TRGB magnitudes. The resulting dis-

tance moduli are shown in the final column of Table 5. The errors in the distances are the random error associated with the TRGB measurement added in quadrature with the 0.07 mag error from the Ferrarese et al. (2000) calibration, resulting in a ~ 0.08 mag random error. The systematic error is approximately 0.15 magnitudes, slightly higher than the Ferrarese et al. (2000) value due to the change in filter system.

Comparing these distances to the literature values compiled in Table 1 reveals good agreement on two galaxies, with less good agreement for the other four. We note that our limit at $F814W_{\text{TRGB}}$ of ~ 25.5 gives a distance modulus limit of ~ 29.6 . Based on previous distance measurements, we do not expect to detect the TRGB in any other galaxies other than those listed in Table 5 except possibly for NGC 891 and NGC 4517, whose non-detection we discussed above.

We now compare our distances with previous distances

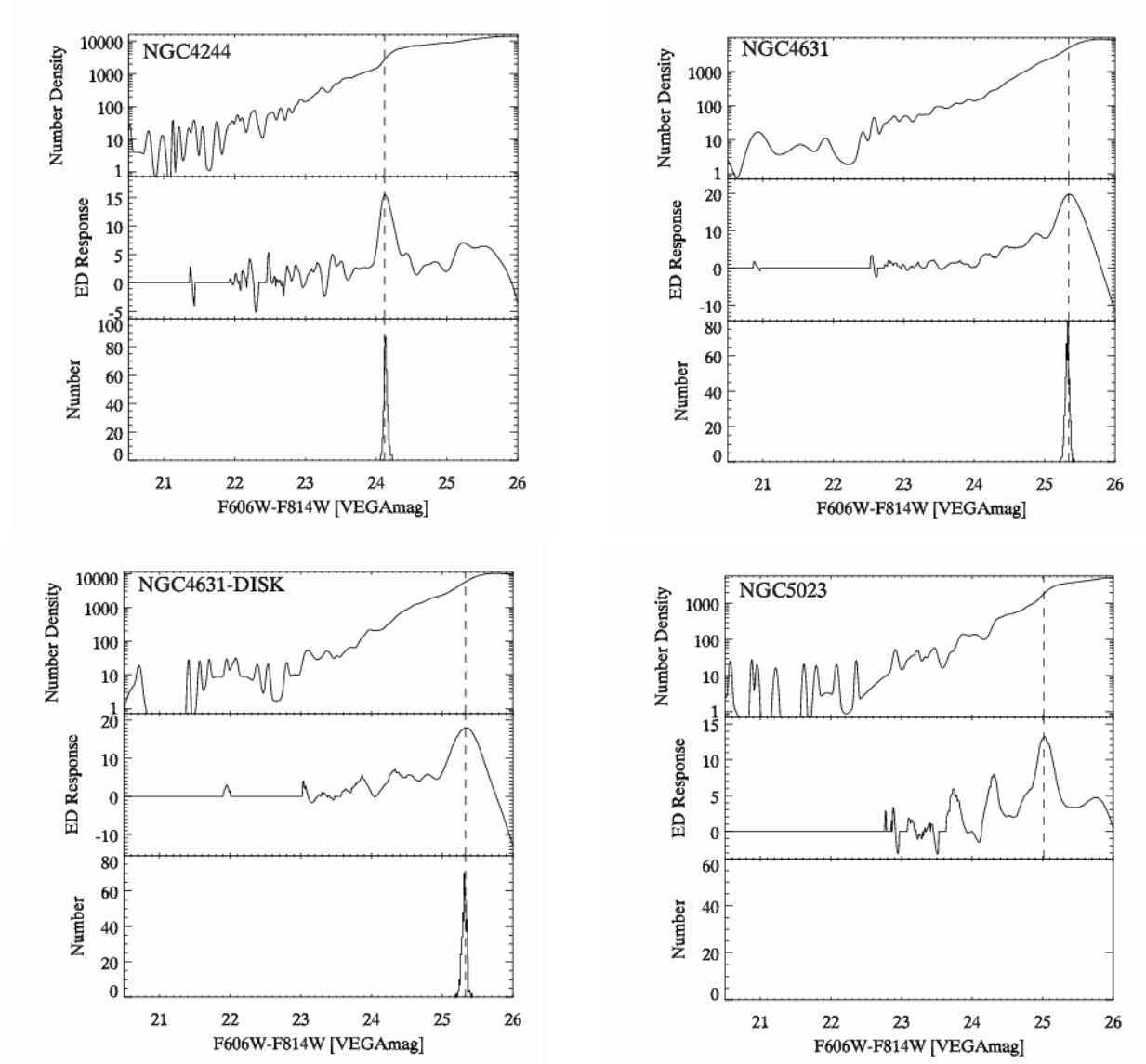
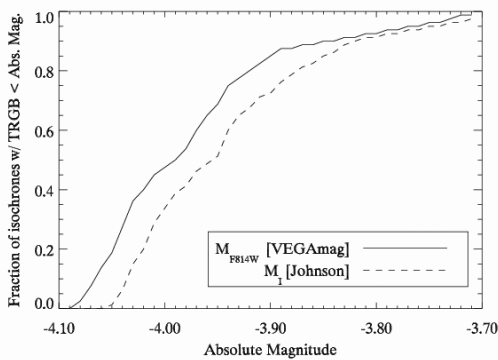
FIG. 7.— *continued*

FIG. 8.— Cumulative distribution of Padova isochrones with TRGB magnitudes brighter than a given absolute magnitude. Solid line shows the distribution for M_{F814W} VEGAmag isochrones, while the dashed line shows the Johnson M_I values.

on a case-by-case basis. The listed $\Delta(m-M)$ value is found by taking our distance modulus and subtracting the previous measurement.

- IC 5052 ($\Delta(m-M)=0.10$): The previous distance measurement is from the IR Tully-Fisher relation as given in Bottinelli et al. (1988). In fact, Bottinelli et al. (1988) gives two values for the distance modulus, calculated using different Tully-Fisher relations, the mean of which gives the distance modulus we have found.
- NGC 55 ($\Delta(m-M)=0.35$): The distance given in Table 1 is from Karachentsev et al. (2003a), who reinterprets older HI Tully-Fisher data collected from various sources by Puche & Carignan (1988) to determine the distance of 1.8 Mpc ($m-M=26.28$). Previous measurements using the magnitudes of supergiants (Pritchett et al. 1987) from ground-based narrow band imaging find an even closer distance of

1.38 Mpc ($m-M=25.7$) which disagrees even more severely with our measured distance. We suggest that these previous measurements may be unreliable, especially the Tully-Fisher relationship in this irregular galaxy. We also note that our distance modulus agrees within the errors to the TRGB & Cepheid distance to NGC 300 (Butler et al. 2004; Freedman et al. 2001), another galaxy in the Sculptor Group. Assuming similar distance moduli, the separation of 8 degrees between these galaxies translates to a physical distance of ~ 300 kpc.

- NGC 4144 ($\Delta(m-M)=1.43$): The Table 1 $m-M=27.93$ value is from the Bottinelli et al. (1988) IR Tully-Fisher relation. Other estimates give wildly varying distances: a previous B band Tully-Fisher distance (Bottinelli et al. 1985) gave $m-M=28.87$, while a brightest star measurement by Karachentsev & Drozdovsky (1998) gives $m-M=29.9$. Our distance measurement falls between these latter two.
- NGC 4244 ($\Delta(m-M)=-0.06$): The close agreement between our distance and the distance in Table 1 is unsurprising because both were derived using the TRGB method from HST data. We note that a previous B-band Tully-Fisher measurement finds $m-M=27.77$ (Bottinelli et al. 1984), ~ 0.5 magnitudes away from the TRGB distance.
- NGC 4631 ($\Delta(m-M)=1.24$): The previous measurement of $m-M=28.18$ is from the B-band Tully-Fisher relation of Bottinelli et al. (1985). Measurements of the HI and CO Tully-Fisher (Schoniger & Sofue 1994) relation suggest an even closer distance modulus of 27.5 to 27.8, in even worse agreement with the TRGB distance. We note that this galaxy is undergoing interactions (Rand 1994) and has nearby companions, both of which could make the Tully-Fisher distances less reliable.
- NGC 5023 ($\Delta(m-M)=0.35$): This difference in $m-M$ is within the very large error (0.5 mag) given by Bottinelli et al. (1985) for the B-band Tully-Fisher measurement of this galaxy.

To provide another check on our distance measurements, we compare our TRGB distances to the K band/ V_{\max} Tully-Fisher relation presented in Verheijen (2001):

$$M_K = -1.62 \pm 0.49 - 8.5 \pm 0.2 \log(2V_{\max}) \quad (1)$$

Figure 9 shows the comparison between this Tully-Fisher relation and the distances we have derived. The magnitudes shown were calculated using the 'total' K_s magnitude (K_{tot} in Table 1) from Jarrett et al. (2003) and our TRGB distances. The V_{\max} values are those shown in Table 1 (Paturel et al. 2003) and represent the maximum circular velocity in that galaxy. We note that K' filter used for deriving the Tully-Fisher relationship has a similar bandpass to the K_s filter used in 2MASS, and so any differences between the magnitude systems should be small. For the six galaxies that we have derived distances to, the scatter around the Tully-Fisher relation is 0.65 magnitudes. This is similar to the 0.71 magnitude scatter around the relation found by Verheijen (2001).

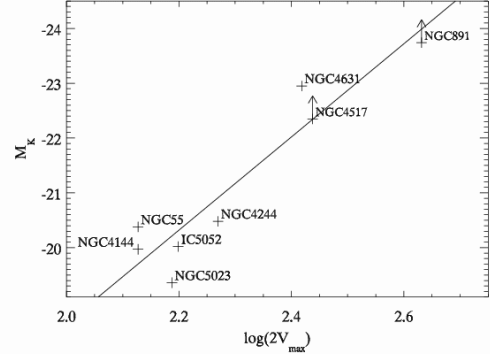


FIG. 9.— A comparison of the derived TRGB distances (data points) vs. the K band Tully-Fisher relation from Verheijen (2001) (line). In addition to the six galaxies with detected distances, we show NGC 891 and NGC 4517 assuming a lower limit to the distance modulus of 29.68.

Overall, we find that there are plausible reasons for the differences between our distances and those previously measured. The agreement found between different fields of the same galaxy as well as the consistency of our TRGB distances with the K band Tully-Fisher relationship and the previous TRGB measurement (NGC 4244) all give us reason to believe the distances given here are more accurate than previous distances found in the literature. We also note that the relative distances between the galaxies should be accurate to within the ~ 0.03 magnitude errors in the TRGB determination.

4.4. Metallicity of the RGB

Table 5 shows the color of the RGB at an absolute magnitude of -3.5 in both the Johnson system, $(V-I)_{-3.5}$ and the ACS VEGAMag system, $(F606W-F814W)_{-3.5}$. These values were found by fitting a Gaussian to the distribution of stars within an 0.2 magnitude band centered at an absolute magnitude of -3.5 (assuming TRGB at $M_{F814W}=-4.08$ and $M_I=-4.06$). The value for $(V-I)_{-3.5}$ has been used by Lee et al. (1993) to derive the metallicity as follows:

$$[\text{Fe}/\text{H}] = -12.64 + 12.6(V-I)_{-3.5} - 3.3(V-I)_{-3.5}^2 \quad (2)$$

The $[\text{Fe}/\text{H}]$ values from this equation are shown in Table 5 and range from -1.2 to -1.7 . Comparison of the $(F606W-F814W)_{-3.5}$ values (Table 1) with Padova isochrones shows similar results, with the data falling just to the metal rich side of the $[\text{Fe}/\text{H}]=-1.3$ isochrone. This confirms that the population of stars we are using for TRGB distance determination are metal poor and suggests that they are part of some kind of halo or thick disk system. Note also that the outer fields of NGC 55 and NGC 4631 have lower metallicities than the inner fields as expected in some disk formation models. We will explore these trends more fully in Paper II.

5. SUMMARY

In this paper we have presented the basic properties and data reduction of a sample of edge-on galaxies observed with ACS camera on HST. We summarize our findings below:

- A number of the sample galaxies are close enough to be partially resolved into stars with an identifiable Red Giant Branch, Asymptotic Giant Branch, Main Sequence, and Helium Burning sequences.
- We identify a candidate dwarf galaxy near NGC 4631 that has a mass, age, and size similar to an OB association, but lies 2 kpc above the disk. We also find LMC stars in the IRAS 06070-6147 field, $\sim 9^\circ$ from the LMC center.
- We determine scale lengths and heights for each galaxy using single-disk fits to K-band 2MASS images.
- TRGB distances are derived to eight fields in six galaxies. These are found to have distance moduli between 26.62 and 29.42.
- The metallicities of the high latitude stars appear to be metal-poor with $[\text{Fe}/\text{H}] < -1$.

This work is the first in a series of papers, the next of which focuses on the stellar populations of the galaxies

as a function of scale height (Paper II). Future work includes a third paper on the star cluster content of the sample galaxies.

The authors would like to acknowledge the help of Tom Jarrett in obtaining 2MASS data, Thomas Brown and Marco Sirianni for their help in obtaining ACS photometric calibrations and Leo Girardi for providing isochrones in the ACS filter system. Additionally we'd like to thank Simone Bianchi, Paul Hodge, Kevin Covey, Vandana Desai, Peter Yoachim, and our referee for helpful discussions and comments. Julianne J. Dalcanton was partially supported by the Alfred P. Sloan research foundation. This research has made use of the NASA/IPAC Extragalactic Database (NED) which is operated by the Jet Propulsion Laboratory, California Institute of Technology, under contract with the National Aeronautics and Space Administration. This work was supported by HST-GO-09765.

APPENDIX

K BAND DISK FITS

We describe here the fits performed on 2MASS K band images to determine a consistent set of structural properties in our galaxies. We obtained 2MASS K band images of each galaxy in our sample from the Large Galaxy Atlas (Jarrett et al. 2003). Only one of the galaxies, NGC 3501, was not in the Large Galaxy Atlas, and this we obtained via the 2MASS Extended Source Image server².

We fit these K band images to an edge-on single disk model from van der Kruit & Searle (1981):

$$\Sigma(R, z) = \Sigma_0(R/h)K_1(R/h_R)\text{sech}^2(z/z_0) \quad (\text{A1})$$

where R and z are the radial and vertical coordinates, Σ_0 is the edge-on central surface brightness, h_R is the radial scale length and z_0 is the vertical scale height of an isothermal stellar population. Note that z_0 is different from an exponential scale height. For this reason we use the $z_{1/2}$ parameter, which gives the height above and below the plane that contains 50% of the K band light to facilitate comparison with other studies. For our adopted profile in Eq. 1, $z_{1/2} = 0.549z_0$.

Before fitting, the 2MASS images were cropped and sources were identified using SExtractor (Bertin & Arnouts 1996). Sources other than the target galaxy were masked and the masked image was fit to the single disk model of Eq. 1 using a Levenberg-Marquardt least-squares fit with a uniform weighting of all the unmasked pixels. For galaxies with obvious bulge components (IRAS 06070-6147, NGC 891, NGC 3501, NGC 4206, NGC 4244, and NGC 4517), we masked out the central portion of the galaxy with a radius between 5 and 50 arcsec depending on the size of the bulge. We attempted to fit a second disk component to the galaxies, but found that it did not increase the quality of the fit. Four galaxies, NGC 55, NGC 4183 and NGC 4631, showed significant asymmetry complicating the fitting process, while one galaxy, NGC 891 had a significant dust lane even at K band. The formal errors on z_0 and h_R were at most 4%, however, the actual errors will in most cases be dominated by source structure in the galaxies.

The results of the single disk fits are shown in Table 1 (RA, Dec and position angle, given E of N) and Table 2 (Σ_0 , h_R , and z_0). Also shown in Table 2 are the ratio of scale length to height h_R/z_0 , the half-light height $z_{1/2}$ and the h_R and z_0 values in parsecs assuming the distances in Tables 1 & 5 (where available, TRGB distances from Table 5 are used). The values for the scale length, h_R , range between $16''$ and $91''$, and in physical coordinates between 0.9 and 7 kpc. For z_0 , the range is $2''$ to $24''$ and 300 to 1100 pc. For comparison the Milky Way has $h \sim 3$ kpc (Klypin et al. 2002) and $z_0 \sim 700$ pc (van der Kruit & Searle 1981). The typical h_R/z_0 values for our galaxies are ~ 4 , similar in value to the Milky Way and the 31 edge-on galaxies presented in Pohlen et al. (2000).

REFERENCES

- Alves, D. R. 2004, *New Astronomy Review*, 48, 659
 Bertin, E., & Arnouts, S. 1996, *A&AS*, 117, 393
 Bottinelli, L., Gouguenheim, L., Paturol, G., & de Vaucouleurs, G. 1984, *A&AS*, 56, 381
 —. 1985, *A&AS*, 59, 43
 Bottinelli, L., Gouguenheim, L., & Teerikorpi, P. 1988, *A&A*, 196, 17
 Brown, T. M., et al. 2003, *ApJ*, 592, L17
 Butler, D. J., Martínez-Delgado, D., & Brandner, W. 2004, *AJ*, 127, 1472
 Dohm-Palmer, R. C., & Skillman, E. D. 2002, *AJ*, 123, 1433

² <http://irsa.ipac.caltech.edu/applications/2MASS/PubGalPS/>

- Dohm-Palmer, R. C., et al. 2002, *AJ*, 123, 813
- Dolphin, A. E., et al. 2003, *AJ*, 126, 187
- Duc, P.-A., & Mirabel, I. F. 1998, *A&A*, 333, 813
- Ferrarese, L., et al. 2000, *ApJ*, 529, 745
- Freedman, W. L., et al. 2001, *ApJ*, 553, 47
- Gallart, C., Stetson, P. B., Hardy, E., Pont, F., & Zinn, R. 2004, *astro-ph/0409023*
- Gavazzi, G., Boselli, A., Scodreggio, M., Pierini, D., & Belsole, E. 1999, *MNRAS*, 304, 595
- Girardi, L., Bressan, A., Bertelli, G., & Chiosi, C. 2000, *VizieR Online Data Catalog*, 414, 10371
- Howk, J. C., & Savage, B. D. 1999, *AJ*, 117, 2077
- Irwin, M. J. 1991, in *IAU Symp. 148: The Magellanic Clouds*, 453
- Jarrett, T. H., Chester, T., Cutri, R., Schneider, S. E., & Huchra, J. P. 2003, *AJ*, 125, 525
- Jensen, J. B., et al. 2003, *ApJ*, 583, 712
- Karachentsev, I. D., & Drozdovsky, I. O. 1998, *A&AS*, 131, 1
- Karachentsev, I. D., et al. 2003a, *A&A*, 404, 93
- Karachentsev, I. D., Karachentseva, V. E., & Parnovskij, S. L. 1993, *Astronomische Nachrichten*, 314, 97
- Karachentsev, I. D., et al. 2003b, *A&A*, 398, 467
- Klypin, A., Zhao, H., & Somerville, R. S. 2002, *ApJ*, 573, 597
- Lee, M. G., Freedman, W. L., & Madore, B. F. 1993, *ApJ*, 417, 553
- Méndez, B., Davis, M., Moustakas, J., Newman, J., Madore, B. F., & Freedman, W. L. 2002, *AJ*, 124, 213
- Odewahn, S. C., & Aldering, G. 1995, *AJ*, 110, 2009
- Paturel, G., Theureau, G., Bottinelli, L., Gouguenheim, L., Coudreau-Durand, N., Hallet, N., & Petit, C. 2003, *A&A*, 412, 57
- Paturel, G., et al. 1995, *LEDA: The Lyon-Meudon Extragalactic Database (ASSL Vol. 203: Information On-Line Data in Astronomy)*, 115–126
- Pohlen, M., Dettmar, R.-J., Lütticke, R., & Schwarzkopf, U. 2000, *A&AS*, 144, 405
- Pritchet, C. J., Schade, D., Richer, H. B., Crabtree, D., & Yee, H. K. C. 1987, *ApJ*, 323, 79
- Puche, D., & Carignan, C. 1988, *AJ*, 95, 1025
- Rand, R. J. 1994, *A&A*, 285, 833
- Sakai, S., Madore, B. F., & Freedman, W. L. 1996, *ApJ*, 461, 713
- Sarajedini, A., & Van Duyne, J. 2001, *AJ*, 122, 2444
- Schlegel, D. J., Finkbeiner, D. P., & Davis, M. 1998, *ApJ*, 500, 525
- Schoniger, F., & Sofue, Y. 1994, *A&A*, 283, 21
- Schweizer, F. 1978, in *IAU Symp. 77: Structure and Properties of Nearby Galaxies*, 279–284
- Seth, A. C., Dalcanton, J. J., & de Jong, R. 2004, to be submitted to *AJ*
- Stetson, P. B. 1987, *PASP*, 99, 191
- Temporin, S., Weinberger, R., Galaz, G., & Kerber, F. 2003, *ApJ*, 587, 660
- Tonry, J. L., et al. 2001, *ApJ*, 546, 681
- Tully, R. B., & Fisher, J. R. 1988, *Annales de Geophysique*
- Tully, R. B., & Pierce, M. J. 2000, *ApJ*, 533, 744
- van der Kruit, P. C., & Searle, L. 1981, *A&A*, 95, 105
- van Dokkum, P. G. 2001, *PASP*, 113, 1420
- Verheijen, M. A. W. 2001, *ApJ*, 563, 694
- Zucker, D. B., et al. 2004, *ApJ*, 612, L121